JGR Space Physics

RESEARCH ARTICLE
10.1029/2021JA029439

Simulations of Energetic Neutral Atom Sputtering From Ganymede in Preparation for the JUICE Mission

A. Pontoni[1], M. Shimoyama[1], Y. Futaana[1], S. Fatemi[2], A. R. Poppe[3], M. Wieser[1], and S. Barabash[1]

[1]Swedish Institute of Space Physics, Kiruna, Sweden, [2]Department of Physics at Umeå University, Umeå, Sweden, [3]Space Sciences Laboratory, University of California, Berkeley, CA, USA

Key Points:

- A new method for calculating sputtered fluxes at Ganymede is introduced
- The energy spectra of sputtered H_2O, O_2, and H_2 Energetic Neutral Atoms (ENAs) are calculated for the first time
- The Jovian Neutrals Analyzer on JUpiter ICy moon Explorer (JUICE) can remotely map ion precipitation at Ganymede

Correspondence to:

A. Pontoni,
angele.pontoni@irf.se

Citation:

Pontoni, A., Shimoyama, M., Futaana, Y., Fatemi, S., Poppe, A. R., Wieser, M., & Barabash, S. (2022). Simulations of energetic neutral atom sputtering from Ganymede in preparation for the JUICE mission. *Journal of Geophysical Research: Space Physics*, *127*, e2021JA029439. https://doi.org/10.1029/2021JA029439

Received 14 APR 2021
Accepted 7 DEC 2021

Abstract Jovian magnetospheric plasma irradiates the surface of Ganymede and is postulated to be the primary agent that changes the surface brightness of Ganymede, leading to asymmetries between polar and equatorial regions as well as between the trailing and leading hemispheres. As impinging ions sputter surface constituents as neutrals, ion precipitation patterns can be remotely imaged using the Energetic Neutral Atoms (ENA) measurement technique. Here we calculate the expected sputtered ENA flux from the surface of Ganymede to help interpret future observations by ENA instruments, particularly the Jovian Neutrals Analyzer (JNA) onboard the JUpiter ICy moon Explorer (JUICE) spacecraft. We use sputtering models developed based on laboratory experiments to calculate sputtered fluxes of H_2O, O_2, and H_2. The input ion population used in this study is the result of test particle simulations using electric and magnetic fields from a hybrid simulation of Ganymede's environment. This population includes a thermal component (H^+ and O^+ from 10 eV to 10 keV) and an energetic component (H^+, O^{++}, and S^{+++} from 10 keV to 10 MeV). We find a global ENA sputtering rate from Ganymede of 1.42×10^{27} s^{-1}, with contributions from H_2, O_2, and H_2O of 34%, 17%, and 49% respectively. We also calculate the energy distribution of sputtered Energetic Neutral Atoms (ENAs), give an estimate of a typical JNA count rate at Ganymede, and investigate latitudinal variations of sputtered fluxes along a simulated orbit track of the JUICE spacecraft. Our results demonstrate the capability of the JNA sensor to remotely map ion precipitation at Ganymede.

Plain Language Summary Particles trapped by Jupiter's magnetic field interact with Jupiter's moons. Ganymede, the largest of those moons, lacks a dense atmosphere to protect its surface from these energetic Jovian particles, but Ganymede's magnetic field is strong enough to influence their trajectory: charged particles are deflected away from equatorial regions to polar regions, resulting in uneven particle precipitation patterns at the surface of Ganymede. When ions hit the surface of Ganymede, they eject particles from the surface, in a process referred to as sputtering. Those particles are mostly neutral and therefore unaffected by Ganymede's magnetic fields, so we can image where ions hit the surface of Ganymede by measuring ejected neutral particles. The Jovian Neutrals Analyzer (JNA) will fly onboard the JUpiter ICy moon Explorer (JUICE) spacecraft and will measure sputtered neutrals in the vicinity of Ganymede. To help interpret the data to be collected by JNA, we used models derived from laboratory experiments to simulate what JNA will observe at Ganymede. Our results show that JNA will be able to show us where ions hit the surface of Ganymede, which is important as uneven ion precipitation is thought to explain why Ganymede's poles are brighter than its equatorial regions.

1. Introduction

Imaging plasma precipitation patterns at the surface of Ganymede is a key measurement for understanding the effect of Jovian plasma precipitation on the brightness and composition of the surface. Ganymede stands out as Jupiter's largest moon and also the only moon in the Solar System to feature an intrinsic magnetic field, causing the formation of a small magnetosphere inside Jupiter's much larger magnetosphere. Ganymede's magnetic field locally impedes or enhances Jovian plasma access to its surface, resulting in variable precipitation patterns (Fatemi et al., 2016; Khurana et al., 2007; Plainaki et al., 2020; Poppe et al., 2018). Precipitating ions can be backscattered by the surface or cause surface constituents and radiolytic products to sputter. Backscattered and sputtered particles leave the surface mainly as neutral and with energies ranging from eV to MeV (Johnson, 1990).

Such neutral particles are usually referred to as Energetic Neutral Atoms (ENAs) (Gruntman, 1997). ENAs are well-known populations in the terrestrial magnetosphere (Roelof, 1987). They originate from ions neutralized by charge-exchange with neutrals, and are used to probe distant plasma in space. The trajectories of ENAs are not influenced by electric or magnetic fields and therefore preserve information about their original velocity, assuming that the gravitational force is negligible. Thus ENA measurements can and have been used to remotely map ion precipitation on airless bodies, where in situ precipitating ion observation is not easily possible. For example, backscattered solar wind protons and sputtered oxygen atoms were observed at the Moon by the Interstellar Boundary EXplorer (IBEX) (Allegrini et al., 2013; McComas et al., 2009) and by CENA on Chandrayaan-1 (Futaana et al., 2013; Vorburger et al., 2014; Wieser et al., 2016). Ganymede will also be visited by an ENA instrument: the Jovian Neutrals Analyzer (JNA) will fly on-board the JUpiter ICy moon Explorer (JUICE) spacecraft.

To help interpret the data collected by JNA, estimates of ENA fluxes are needed. However, estimating ENA fluxes requires modeling the sputtering process. The sputtering process has been widely studied because of its relevance for icy bodies such as Ganymede, Europa, and Enceladus. Their lack of a dense atmosphere leaves their surface exposed to ion precipitation, leading to the sputtering of surface constituents and radiolytic products. Along with other processes such as sublimation and photo-stimulated desorption, sputtering contributes to the creation of a neutral exosphere on several bodies (Cassidy et al., 2010; Cooper, 2001; Johnson et al., 2004; Marconi, 2007; Wurz et al., 2010).

While a comprehensive analytical description of the sputtering process is not currently available, sputtering has been extensively studied through laboratory experiments (Baragiola et al., 2003; Famá et al., 2008; Galli et al., 2017, 2018; Teolis et al., 2017). Several methods have been developed to calculate the sputtering yield of ions on icy surfaces as a function of projectile energy and species, incidence angle, and surface temperature (Famá et al., 2008; Johnson et al., 2004; Teolis et al., 2017). Such methods, or combinations of them, have been used extensively to simulate surface-plasma interactions at Europa (Plainaki et al., 2010, 2012; Vorburger & Wurz, 2018) and Ganymede (Leblanc et al., 2017; Marconi, 2007; Plainaki et al., 2015, 2020; Poppe et al., 2018; Shematovich, 2016; Turc et al., 2014).

Here, we estimate sputtered ENA fluxes at the surface of Ganymede by applying models formulated by Famá et al. (2008), Johnson et al. (2004) and Teolis et al. (2017) to a population of incident Jovian plasma obtained through hybrid simulations by Poppe et al. (2018). This allows us to calculate the expected sputtered ENA fluxes of H_2O, H_2, and O_2 and to further apply the Thompson-Sigmund law expressed in Vorburger and Wurz (2018) to calculate their energy distribution. By convolving JNA's estimated geometric factor with the energy distribution, we give an expected JNA count rate in the vicinity of Ganymede. Finally we investigate latitudinal variations of the sputtered ENA fluxes by simulating a simplified orbit of the JUICE spacecraft around Ganymede.

2. Materials and Methods

2.1. Input Population

The incident ion population is taken from a combination of three-dimensional hybrid simulations of Ganymede's magnetosphere and subsequent backwards-Liouville particle tracing through the hybrid electromagnetic fields (Fatemi et al., 2016; Poppe et al., 2018). They simulated the ion velocity distribution for the Galileo G8 flyby, when Ganymede was in the Jovian plasma sheet. The incident population used as an input for calculating the sputtered ENA flux in this study is comprised of three-dimensional velocity distribution functions for thermal O^+ and H^+ from 10 eV to 10 keV and energetic H^+, O^{++} and S^{+++} from 10 keV to 10 MeV. The spatial resolution of the hybrid model is $1° \times 1°$ in latitude and longitude at the surface of Ganymede.

Figure 1 shows the resulting plasma precipitation pattern, that is, a map of the ion flux integrated over all incident species, energies and angles. On the trailing hemisphere (180°–360°W) of the equatorial regions, Ganymede's surface is shielded from Jovian plasma by Ganymede's intrinsic magnetic field. In contrast, intense precipitation is observed on the leading hemisphere of the equatorial regions (0°–180°W), where plasma is accelerated back toward Ganymede by reconnection in the magnetotail (Fatemi et al., 2016; Poppe et al., 2018). The most intense flux is observed in the high-latitude cusp regions on the leading hemisphere, where open-closed magnetic field lines boundaries are located (±50°–60° in latitude) (Poppe et al., 2018).

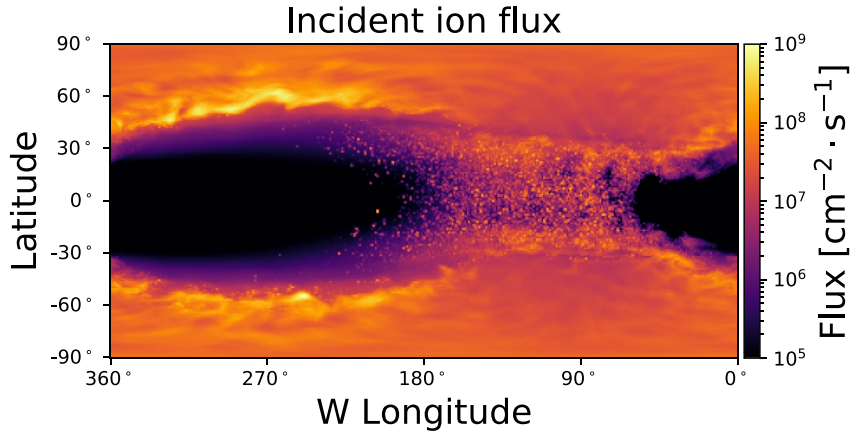

Figure 1. Incident ion flux at the surface of Ganymede, taken from Poppe et al. (2018) and integrated over all species, angles and energies. The leading hemisphere extends from 0°W to 180°W, while the trailing hemisphere extends from 180°W to 360°W. For our study here, we choose a single period along Ganymede's orbit such that the sub-solar point is located at 270°W, that is, the corotating plasma flow is aligned with the sunlight direction.

Figure 2 shows the energy distribution of the incident ion flux at Ganymede's surface resulting from Poppe's backwards-Liouville tracing model. The flux was integrated over all incident angles and averaged over the surface of Ganymede. Two components can be identified: (a) the thermal component comprised of plasma from Io's torus diffusing outwards (Siscoe & Summers, 1981); (b) the energetic component originating from accelerated Io torus plasma and solar wind plasma diffusing inwards (Siscoe et al., 1981).

2.2. Sputtering Yield

Ion sputtering on water ice has been extensively studied via laboratory experiments and the sputtered products are known to be comprised of H_2O, H_2, and O_2 (Galli et al., 2017; Johnson et al., 2004). While H_2O is a surface constituent directly sputtered by the impact of ions on water ice, H_2 and O_2 are radiolytic products generated in the material by the irradiation of water ice and subsequently sputtered by projectiles (Johnson et al., 2003; Paranicas et al., 2009; Teolis et al., 2017). Here we use three different functions to calculate the sputtering yield, depending on the energy of the incident ions and the sputtered species. Throughout the paper, the sputtering yield of a sputtered species *by* an incident species refers to the number of particles of the sputtered species released from the surface by one incident ion.

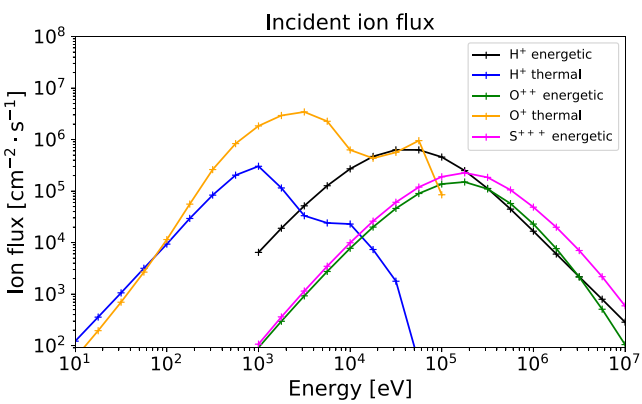

Figure 2. Energy spectra of the precipitating ions used as our input ion populations, integrated over all incident angles and averaged over the surface of Ganymede.

At incident ion energies higher than 100 keV, we use the model described in Johnson et al. (2004) to calculate $Y_{H_2O,high}$, the yield of H_2O as a function of the energy and species of the incident ion:

$$\frac{1}{Y_{H_2O,high}(v,Z)} = \frac{1}{11.2\,Z^{2.8}(v/Z^{1/3})^{-2.24}} + \frac{1}{4.2\,Z^{2.8}(v/Z^{1/3})^{2.16}}, \quad (1)$$

where Z is the atomic number of the incident particle and v the velocity of the incident particle in atomic units (1 au = $2.18 \cdot 10^8$ cm s^{-1}).

At incident ion energies lower than 100 keV, we use the model described in Famá et al. (2008) to calculate $Y_{H_2O,low}$, the yield of H_2O as a function of the energy, species, and incident angle of the incident particle:

$$Y_{H_2O,low}(E,m,Z,\beta) = \frac{1}{U_0}\left(\frac{3}{4\pi^2 C_0 \alpha S_n} + \eta S_e^2\right)\cos^{-f}(\beta), \quad (2)$$

where E, m, and Z are respectively the energy, mass, and atomic number of the projectile. β is the incidence angle, defined from the surface normal. At low-energies, where elastic sputtering processes dominate, the yield is

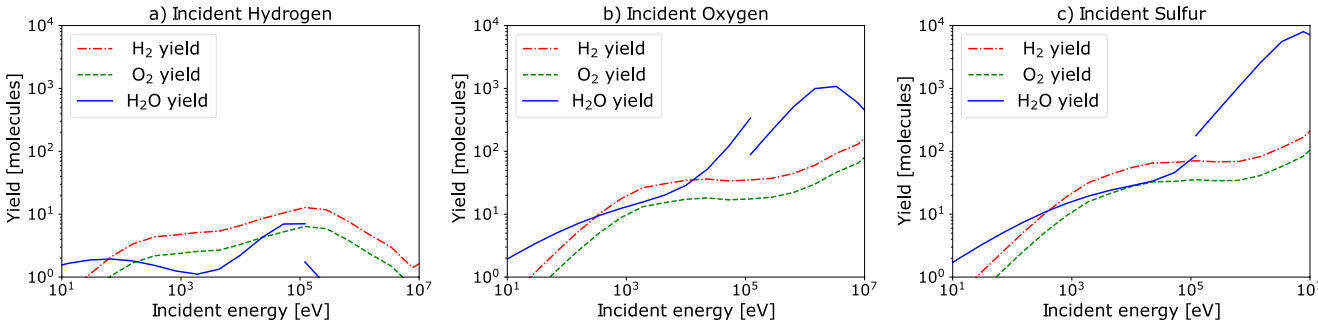

Figure 3. Sputtering yield of H_2O, H_2, and O_2 by incident (a) H, (b) O, and (c) S ions. The discontinuity at 100 keV for the H_2O yields is explained by the transition of the model from Famá's to Johnson's. The yields of H_2 and O_2 are calculated using only Teolis' model.

inversely proportional to the nuclear-stopping cross section S_n. At high energies, where electronic processes dominate, the yield is proportional to the squared electronic-stopping cross section S_e. Details about the other constants (U_0, C_0, α, η, and f) can be found in Famá et al. (2008).

In Equation 2, we do not include the temperature-dependent component of Famá's model, as it is attributed to H_2 and O_2 produced by radiolysis, a temperature-dependent process. Instead, we calculate the yield of H_2 ($Y_{H_2}(E,\ T,\ \beta)$) and that of O_2 ($Y_{O_2}(E,\ T,\ \beta)$) using the model derived by Teolis et al. (2017):

$$Y_{O_2}(E,T,\beta) = \frac{Y_{H_2}(E,\ T,\ \beta)}{2} = \epsilon g^0_{O_2} x_o \left[1 - \exp\left(-\frac{r_o \cos(\beta)}{x_o}\right)\right]\left[1 + q_o \exp\left(-\frac{Q}{k_b T}\right)\right] / r_o \cos(\beta), \quad (3)$$

where T is the temperature of the surface of Ganymede, β the incidence angle of the projectile measured from the surface normal, and k_b is the Boltzmann constant. Details about ϵ, $g^0_{O_2}$, x_0, r_0, q_0, and Q can be found in Teolis et al. (2017). The temperature model used in this study was derived by Marconi (2007) based on data from the Galileo spacecraft (Orton et al., 1996). The dayside temperature is given by $T(\lambda) = 70\ \cos(\lambda)^{0.75} + 80$ K (where λ is the subsolar latitude) and the nightside temperature is a constant 80 K.

Figure 3 shows the sputtering yield of H_2O, O_2, and H_2 by O, H, and S ions impinging on water ice. The discontinuity at 100 keV for the H_2O yields is due to the transition of the model from Famá's to Johnson's. We chose 100 keV as the threshold for the transition based on work by Cassidy et al. (2013), but our results are not sensitive to the threshold energy. Generally, the H_2O yield by O and S is higher than 1 and increases with energy for most of the energy range shown here. Because of its low atomic mass, the yield by H is much lower. A surface temperature of 124 K was used to generate these figures, which corresponds to an average daytime disk temperature (Grundy et al., 1999). As mentioned above, the actual surface temperature used in our model varies between 80 K on the nightside and 150 K at the subsolar point.

2.3. Sputtered Energy Distribution

We assume a Thompson-Sigmund law to calculate the probability distribution $S(K)$ of the energy of the sputtered particles, expressed in (Vorburger & Wurz, 2018) as:

$$S(K) = \frac{6E_b}{3 - 8\sqrt{K/E_i}} \frac{K}{(K + E_b)^3} \cdot \left(1 - \sqrt{\frac{K + E_b}{4\ E_i (M_1 M_2)/(M_1 + M_2)^2}}\right), \quad (4)$$

where K is the energy of the sputtered neutral particle, E_b the binding energy of the surface (0.054 eV as also used in Plainaki et al., 2015), E_i the energy of the projectile, and M_1 and M_2 are the masses of the projectile and sputtered neutral particle.

Figure 4a shows the energy distribution of H_2O molecules sputtered by H, O and S with an incident energy of 100 keV. The main consequence of the difference in atomic mass is the cutoff energy of sputtered particles: sputtered H has a cutoff energy of about 20 keV, much lower than the cutoff energy of heavier oxygen and sulfur at about 90 keV. Figure 4b shows the energy distribution of H_2O, H_2, and O_2 molecules sputtered by 100 keV

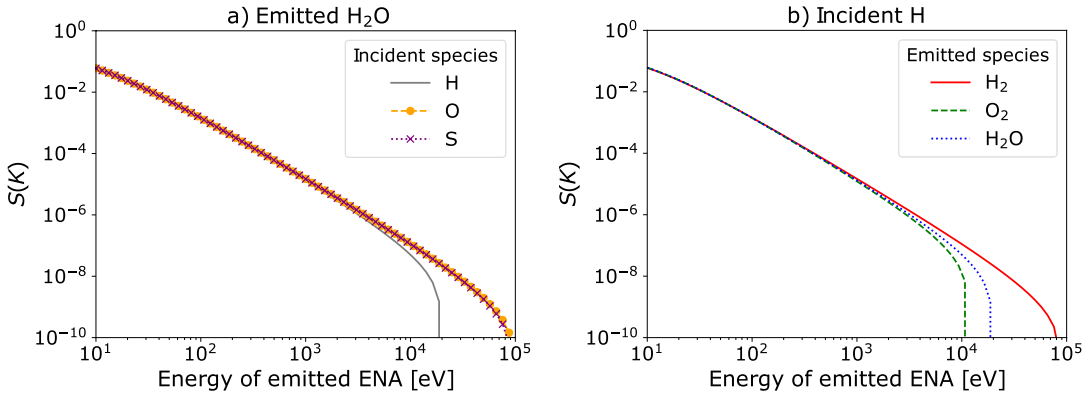

Figure 4. (a) Probability distribution of the energy of H_2O sputtered by different incident species. (b) Probability distribution of the energy of H_2O, H_2, and O_2 molecules sputtered by H, for incident energies of 100 keV.

H. Higher masses result in lower cutoff energies, with respective cutoff energies for O_2, H_2O, and H_2 of about 10 keV, 20 keV, and 80 keV.

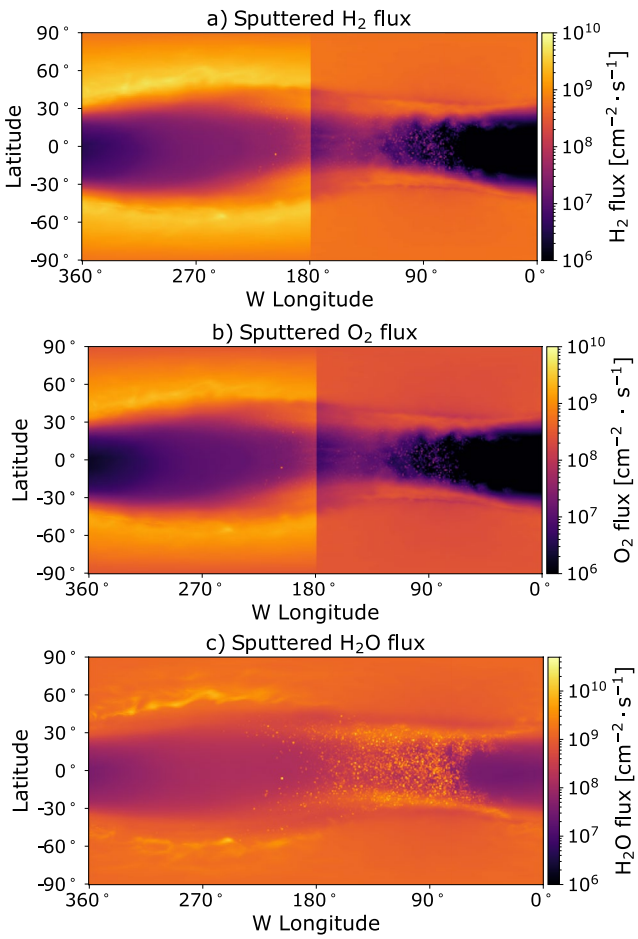

Figure 5. Maps of the sputtered fluxes of H_2, O_2, and H_2O, integrated over all incident species, energies, and angles.

2.4. Flux Calculation

The differential flux of the sputtered neutrals, $j(K)$, is calculated from the combination of the above-mentioned parameters, where K is the energy of the sputtered particle. In our model, the incident plasma taken from hybrid simulations is $f(v, \theta, \phi)$, in units of $(m/s)^{-3}$ sr^{-1} cm^{-2} s^{-1}, for each bin at the surface (Poppe et al., 2018), where v is the incident velocity, θ the incident elevation, and ϕ the incident azimuth.

The differential flux $j(K)$ (in units cm^{-2} s^{-1} sr^{-1} eV^{-1}) is calculated using the following expression:

$$j(K) = \frac{1}{2\pi} \int_v \int_\theta \int_\phi f(v,\ \theta,\ \phi)\ Y(E_i)\ S(K; E_i)\ v^2 \cos(\alpha)\sin(\theta)\ dv d\theta d\phi, \quad (5)$$

where E_i the energy of the incident species, $Y(E_i)$ the sputtering yield function, $S(K; E_i)$ the Thompson-Sigmund probability distribution function, and α is the angle between the velocity vector and the local normal vector pointing inward to the center of Ganymede at the corresponding latitude and longitude. We assume that sputtered neutrals are ejected isotropically, and therefore divide the flux by 2π to get the flux per solid angle.

3. Results

3.1. ENA Sputtering Maps

Figure 5 shows the calculated flux maps of the sputtered ENAs (H_2, O_2, and H_2O) integrated over all incident species, incident angles, and energies. The colorbar ranges from 10^6 to 10^{10} cm^{-2} s^{-1} for all three maps. H_2 and O_2 fluxes are about five times higher on the dayside than on the nightside due to the higher surface temperature on the dayside, which results in a higher yield of H_2 and O_2 (Equation 3). As the yield of H_2O is independent of temperature, no significant difference between the dayside and the nightside is observed other than that resulting from the input ion precipitation patterns.

Generally, similar patterns to the ion precipitation map (Figure 1) are observed for ENA sputtering. Indeed, the sputtered ENA flux is higher in the

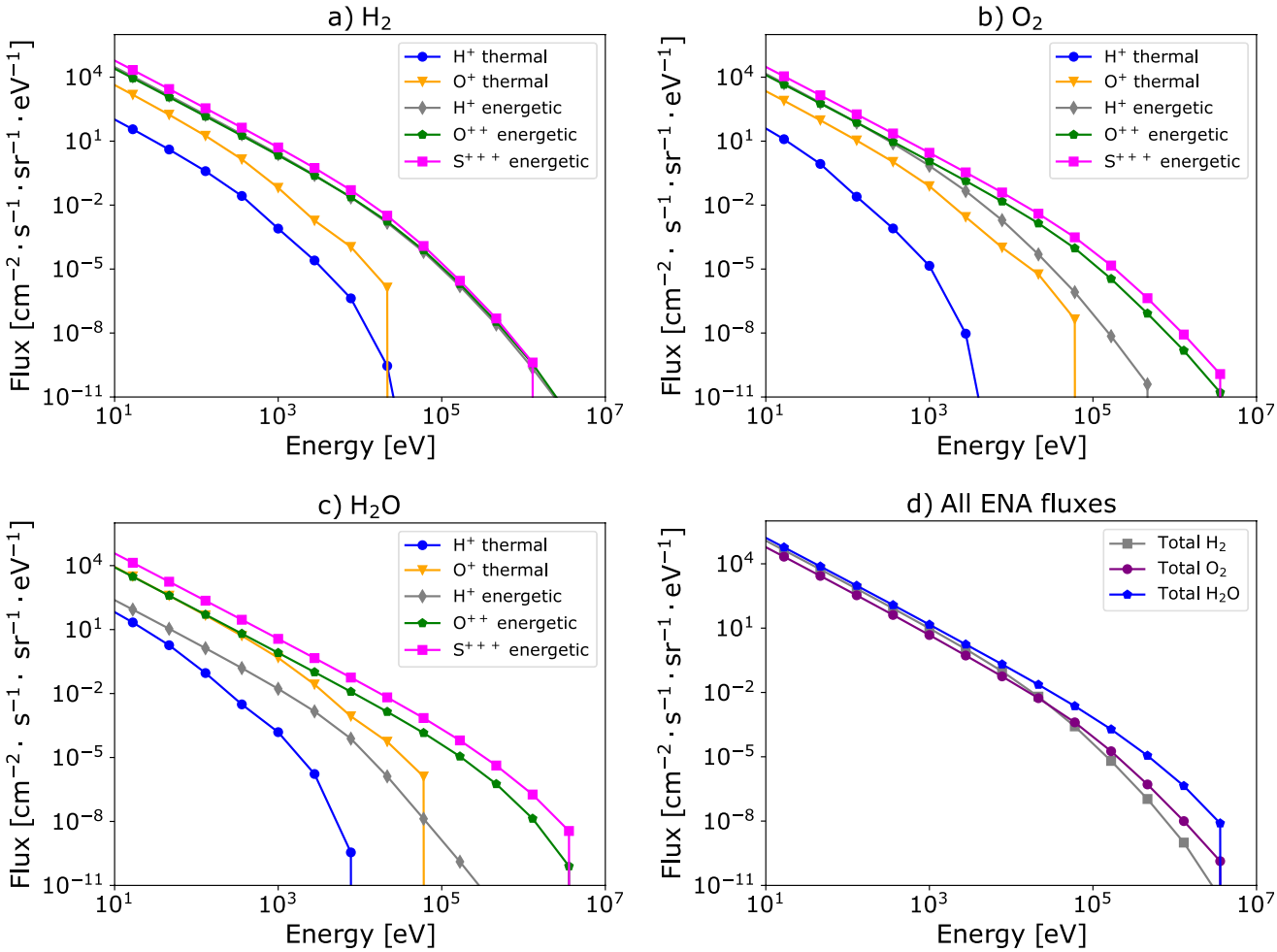

Figure 6. Globally averaged energy distributions of sputtered (a) H_2, (b) O_2, and (c) H_2O, integrated over incident angles and energies. Different colors indicate the incident species which sputtered these Energetic Neutral Atoms (ENAs). (d) Energy distribution of all sputtered species, summed over incident species.

polar regions than in the equatorial regions, and the difference in ENA fluxes between the pole and the equator is more distinct in the trailing hemisphere. The similarity between ion precipitation patterns and sputtering rate patterns illustrates the relevance of the ENA imaging method to remotely map ion precipitation at Ganymede, as previously shown for terrestrial bodies (Allegrini et al., 2013; Futaana et al., 2006, 2013; Vorburger et al., 2014; Wieser et al., 2009).

However, we note an extra feature of the sputtered H_2O flux, observed in neither the incoming ion flux pattern nor for sputtered H_2 and O_2. At equatorial regions on the leading side, the H_2O flux shows significant enhancement, with fluxes of the same order as on the trailing side at the open-close field line boundaries. This enhancement contrasts with the ion flux pattern: at equatorial regions on the leading side, the ion flux is attenuated compared to high-intensity precipitation regions around the open-close field line boundaries. The discrepancy is likely due to the fact that while the ion flux is attenuated, it is also shifted to higher energies. High-energy ions sputter more particles per incident ion and are more efficient at sputtering H_2O than H_2 and O_2. This results in H_2O fluxes at equatorial regions on the leading side comparable with H_2O fluxes at the open-close field line boundaries on the trailing side.

3.2. Sputtered Energy Distribution

Figure 6 shows the energy spectra of sputtered H_2O, H_2, and O_2. Because of the Thompson-Sigmund law (Equation 4) for the energy of sputtered ENAs, fluxes fall as energy increases. Although the incident ion population is

Table 1
Total Sputtering Rate From the Surface of Ganymede Estimated by Previously Published Works as Well as This One

Reference	Input	Sputtering models	Energy range	Sputtered species	Total sputtering rate (s^{-1})
Plainaki et al. (2015)	MHD[a]	Famá[c]	1–100 keV	H_2O, O_2	6.94×10^{25}
Poppe et al. (2018)	Hybrid[b]	Johnson[d]	10 eV–10 MeV	H_2O	7.5×10^{26}
Carnielli et al. (2020)	MHD[a]	Famá[c], Johnson[d]	1 eV–30 MeV	H_2O	2.25×10^{27}
This work	Hybrid[b]	Johnson[d], Teolis[e]	10 eV–10 MeV	H_2O, O_2H_2	1.42×10^{27}

[a]Jia et al. (2008). [b]Fatemi et al. (2016). [c]Famá et al. (2008). [d]Johnson et al. (2004). [e]Teolis et al. (2017).

dominated by the thermal O^+ component at low energies, the contribution of energetic S^{+++} ions to the sputtered H_2O, H_2, and O_2 ENA fluxes dominates over that of all other species across the entire energy range. This is likely a combined effect of the heavier mass of S^{+++} ions, resulting in high sputtering yields, and the fact that the energy distribution of S^{+++} is skewed toward higher energies.

The lowest contribution to sputtered ENAs comes from the thermal H^+ ion component because of their low incident flux (Figure 2) and low sputtering yield, lower than 10 across most of the energy range. For the same reason, energetic H^+ ions contribute the least out of the three energetic species to sputtering O_2 and H_2O. Energetic H^+ ions sputter less H_2O molecules than thermal O^+ ions up to 20 keV. At 20 keV, H_2O ENAs sputtered by O^+ cut off, due to O^+ ions being heavier than H^+ and also contributing more to the incident ion flux.

Total sputtered fluxes of H_2O, H_2, and O_2 are compared with one another in Figure 6d H_2O fluxes dominate over H_2 and O_2 over the entire spectrum, as reflected in the global sputtering rates calculated in Section 3.3.

3.3. Total Sputtering Rate

By integrating the sputtered ENA flux over energy and the entire surface we obtain global sputtering rates of 4.8×10^{26}, 2.4×10^{26}, and 7.0×10^{26} molecules per second for H_2, O_2, and H_2O respectively. This results in a total sputtering rate of 1.42×10^{27} molecules per second. Table 1 shows a comparison of our estimated sputtering rate with previous works. Given from left to right are the model reference, the input plasma model type (MHD or hybrid), the sputtering model(s), the energy range of the sputtered molecules, the species of the sputtered molecules, and the total sputtering rate.

All works give similar results within two orders of magnitude. The difference between our result and those of previous works can be qualitatively explained as follows. Plainaki et al. (2015) derived their ion population using electric and magnetic fields obtained with MHD simulations by Jia et al. (2008). Their energy range covered only 1–100 keV, which is narrower than in this study, leading to a total sputtering rate one order of magnitude lower than ours. They used Famá's model to calculate the yield of H_2O and O_2, but did not account for the sputtering of H_2.

Poppe et al. (2018), when they published the results of the hybrid simulation of Jovian plasma which were used in this study, took the opportunity to estimate the H_2O ENA sputtering rate using Johnson's model. However, at incident energies lower than 100 keV, Johnson's model underestimates the yield, which is better reproduced by Famá's (Cassidy et al., 2013). Moreover, Poppe et al. (2018) considered only the sputtering of H_2O, whereas we considered O_2 and H_2 in addition to H_2O.

Carnielli et al. (2020) used the model in Jia et al. (2008) also used to derive their input ion population, but considered energies ranging from 1 eV to 30 MeV, a wider energy range than used here. Moreover, they considered the contribution of Ganymede's ionospheric ions, which they showed can contribute to up to 10% of the ENA sputtering rate. Their ionospheric ion population was comprised of O_2^+, O^+, H_2O, H_2^+, H^+, and OH^+ with energies ranging from 10 eV to 10 keV. As our input population did not include ionospheric ions and covered a narrower energy range, our total sputtering rate is expected to be lower than theirs.

Our results suggest that H_2 and O_2 account for half of the total neutral sputtering rate from the surface of Ganymede, showing that their contribution should be considered in addition to that of H_2O.

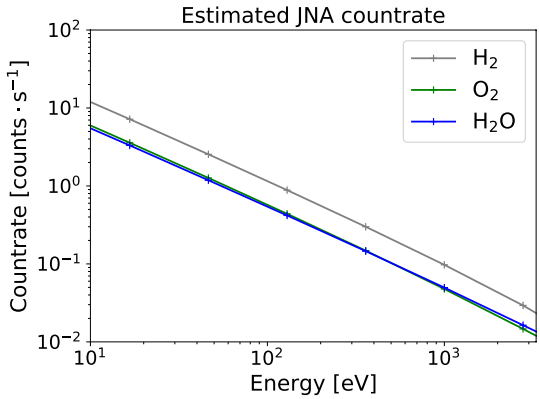

Figure 7. Simulated Jovian Neutrals Analyzer (JNA) count rate as a function of energy for sputtered H_2O, O_2, and H_2 in the energy range JNA can measure.

3.4. JNA Count Rate Estimation

The JUICE spacecraft, planned to launch in 2022 and expected to reach Jupiter in the 2030s, carries the Particle Environment Package (PEP). PEP is comprised of six sensors tailored to study how Jovian plasma interacts with Ganymede's magnetosphere, tenuous atmosphere, and icy surface. In particular, the Jovian Neutrals Analyzer (JNA) will measure ENAs in the Jovian environment in the energy range between 10 eV and 3.3 keV, with a field-of-view of 15° in elevation and 150° in azimuth, divided into 11 pixels (Shimoyama et al., 2018). JNA takes heritage from the CENA instrument family (Barabash et al., 2009; Kazama et al., 2007), and measures ENAs using: (a) a deflection/collimation system that repels ions up to 9 kV (b) a conversion surface for neutral to ion conversion (c) a wave system for energy analysis (10 eV–3.3 keV range with 100% energy resolution) (d) a Time-Of-Flight (TOF) cell that measures the velocity of the particle.

Here we estimate the count rate that JNA is expected to observe at Ganymede by multiplying the flux calculated in Section 3.2 by JNA's estimated geometric factor, GF = 10^{-5} cm^2 sr eV/eV. Figure 7 shows simulated JNA count rates as a function of energy. The geometric factor we used is constant across the energy range, so the count rate distribution follows the Thompson-Sigmund law applied to the sputtered ENAs, resulting in count rates as high as 10^1 counts s^{-1} at 20 eV and as low as 10^{-2} counts s^{-1} at 3.3 keV. JNA is optimized to measure small fluxes, that is, low count rates, even in the harsh radiation environment expected at Jupiter. To achieve this, two Channel Electron Multipliers (CEMs) form a coincidence system for each JNA sector. After hitting the start surface, the particle of interest is detected by one CEM (referred to as STOP CEM), and the associated secondary electron by a different CEM (referred to as START CEM). With this technique, foreground counts can be distinguished from background counts that only trigger signals on one CEM at a time, given that background counts on START and STOP CEMs are not correlated. The expected accidental coincidence count rate, in Jupiter's harsh environment, is < 0.4 count per second.

Despite the optimization to low count rates described above, the spectra in Figure 7 suggests that longer integration times are needed at high energies than at low energies, an important consideration for operations planning and future data analysis. As we did not account for any dissociative processes of the sputtered ENAs, we assume here that H_2, O_2, and H_2O are observed and detected by JNA as molecules. In reality, any molecule entering JNA would most likely be dissociated upon encountering JNA's conversion surface (Wieser et al., 2016), as JNA uses a charge conversion surface to ionize ENAs in order to analyze their energy and guide them to JNA's detectors (Kazama et al., 2007). Since dissociated products would each leave the conversion surface with less energy than the original molecule, the assumption that JNA observes molecules likely gives an underestimation of the count rate JNA would measure at low energies.

3.5. JNA Simulated Observation

To illustrate JNA's ability to measure the variability of Jovian plasma precipitation at Ganymede, we calculate the differential ion flux at different latitudes on Ganymede. In Figure 8, the JUICE spacecraft is assumed to orbit Ganymede at an altitude of 490 km (the lowest circular orbit of the nominal JUICE mission) along the 90°W and 270°W meridians. At four locations along the orbital track, the flux was averaged over areas corresponding to the size of the footprint of JNA's center pixel. Those areas are referred to as zones. For each zone, the fluxes of sputtered H_2, O_2, and H_2O are shown, as well as the JNA one count level for the energy range where JNA can measure. The one count level represents the flux needed for JNA to register 1 coincidence count. It was calculated using JNA's estimated geometric factor, with the assumption that the integration time is 40 s (around the time that it would take JNA to move from one JNA projected pixel to the next).

Zone 1 is situated at Ganymede's north pole and covers areas on both the dayside and the nightside. Zone 2 is centered around the subsolar point. Zone 3 is located along the sub-solar longitude at latitude 60°N, near the open-closed field-line boundary where the ion flux peaks. Zone 4 is centered around the anti-solar point on the nightside.

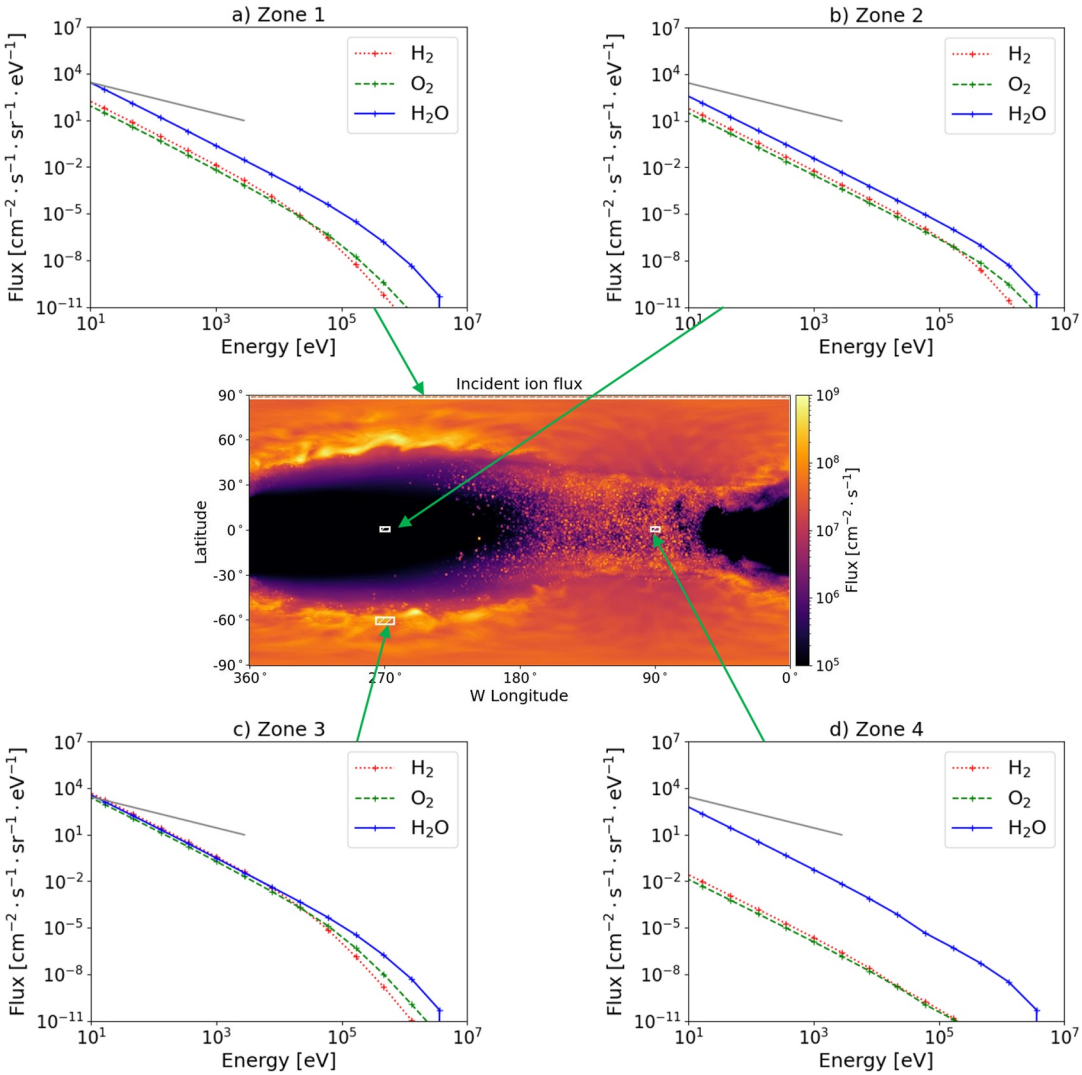

Figure 8. Flux of sputtered H_2, O_2, and H_2O at four locations on the surface of Ganymede, integrated over incident angles and energies. White rectangles show the area over which the flux was averaged and correspond to the footprint of Jovian Neutrals Analyzer (JNA) at 490 km above the surface of Ganymede. The solid gray line indicates the one count level of the JNA instrument for the energy range that JNA can measure (10 eV–3.3 keV).

Figure 8c shows that the highest flux is observed in Zone 3, reflecting the peak in ion flux at this location near the open-closed field-line boundary where both energetic and thermal plasma have easy access to the surface. The ion population there is dominated by thermal O^+ (see Poppe et al., 2018 for incident ion flux distributions at different regions on Ganymede). Zone 1, over the north pole, is exposed to an ion population similar to that in Zone 3, although precipitation at the poles is less intense. Consequently, the ENA flux is lower in Zone 1. Zone 2 is centered around the sub-solar point, where the incident ion flux is three orders of magnitude lower than in Zone 3, as Ganymede's magnetic field prevents low energy Jovian plasma from accessing the surface. The ion flux in Zone 2 is therefore dominated by energetic species, which are more efficient at sputtering H_2O than H_2 and O_2 (see Figure 3). This explains why the sputtered H_2O flux is about one order higher than that of H_2 and O_2. Figure 8d shows an even larger gap between H_2O fluxes and H_2 and O_2 fluxes but there the cause is different. In Zone 4, the ion flux includes contributions of both thermal and energetic species. However, Zone 4 is located on the nightside where the surface temperature is 80 K, which leads to much lower sputtering yields for H_2 and O_2 than for H_2O.

In Zone 1 and 3, at the lower end of JNA's energy range (10–20 eV), sputtered ENA fluxes are high enough to trigger several counts per sector during one pass of JNA over an area as little as little as 2° in latitude. Above

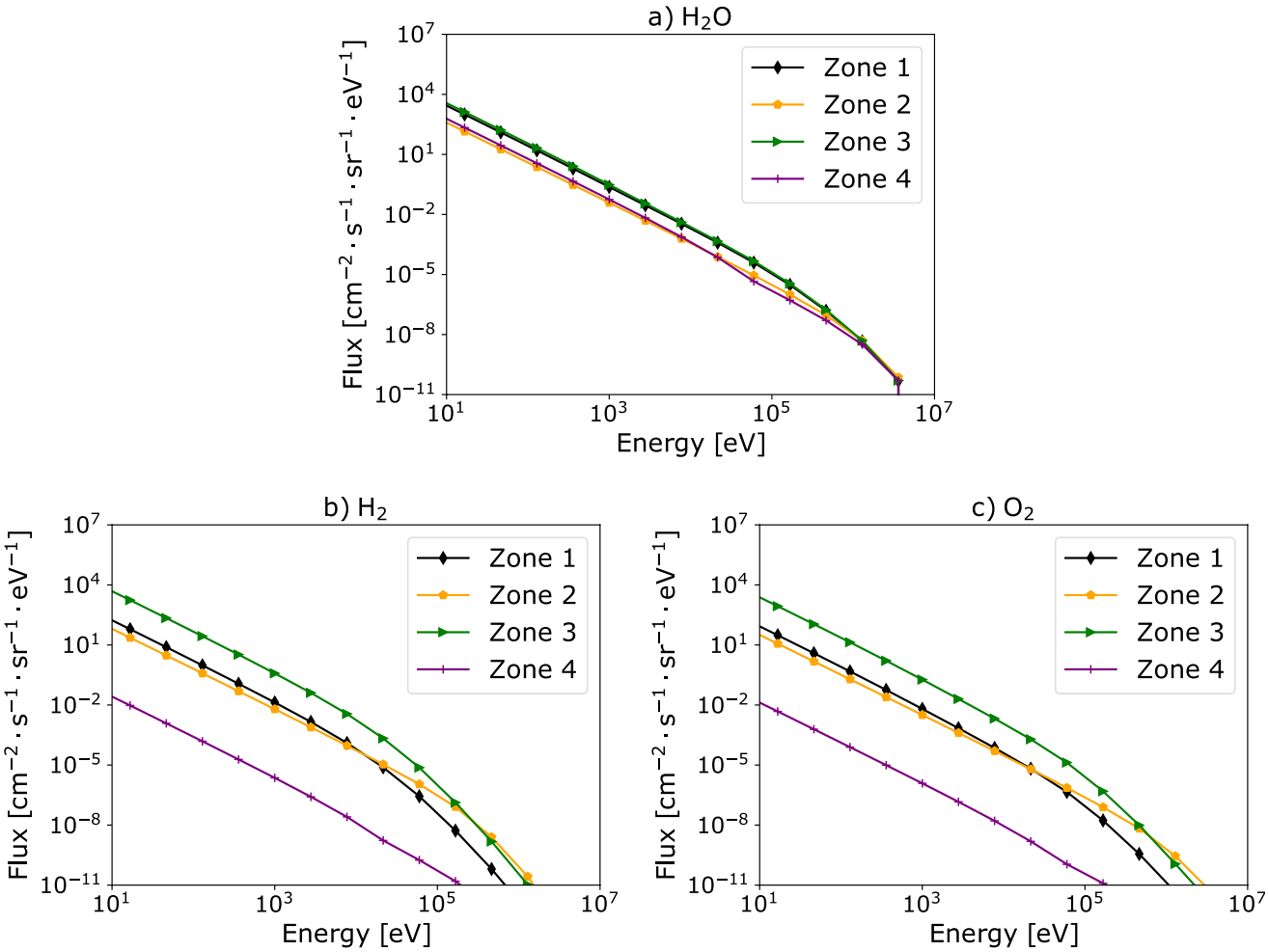

Figure 9. Sputtered H_2O fluxes for all zones, integrated over incident species, energies, and angles.

10–20 eV for Zone 1 and 3, and for most of JNA's measuring range for Zone 2 and 4, sputtered fluxes fall below the one count level, implying that longer integration times (i.e., decrease in spatial resolution) or repeated observations in similar conditions would be needed. The need for longer integration times in Zone 2 and 4 than Zone 1 and 3 will accentuate the effect of polar regions being better resolved than equatorial regions, since JUICE will orbit Ganymede on a polar orbit that will yield more opportunities to perform measurements over polar regions than over equatorial regions.

As sputtered fluxes of H_2O are not temperature-dependent, their variation is a direct result of the differences between the incident sputtering populations. We plot them together in Figure 9a for easier comparison. Despite their different ion populations, all zones show similar fluxes within one order of magnitude. As expected, the highest fluxes are observed over Zone 3 near the open/closed field line boundary while the lowest fluxes are seen over Zone 2 and 4. The picture is different for sputtered H_2 and O_2 (Figures 9b and 9c). There, Zone 4 (on the nightside) shows by far the lowest sputtered fluxes, due to the temperature dependence of the sputtering yield of H_2 and O_2.

In Figure 10, JNA is also assumed to orbit Ganymede at 490 km along the 90°W and 270°W meridians but here we divide the orbit track into 120 zones covering 3° each in latitude (corresponding to the width of JNA's center pixel in elevation). The flux for each latitude zone is shown, for the energy range that JNA can measure (between 10 eV and 3.3 keV) and integrated over sputtered species and incident species, angles, and energies.

Generally, Figure 10 shows that the flux of sputtered ENAs varies by about four orders of magnitude along the simulated trajectory of JNA for all energy bins in the JNA measuring range. Again, we observe that the variability

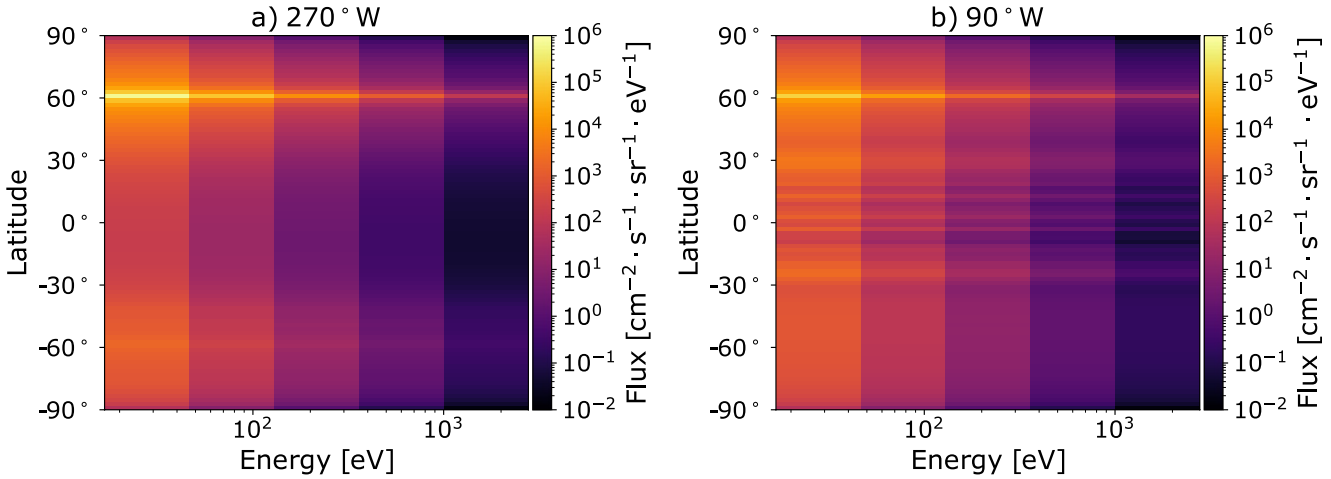

Figure 10. Flux of sputtered Energetic Neutral Atoms (ENAs) integrated over sputtered species and incident species, angles, and energies, shown for each latitude zone corresponding to a Jovian Neutrals Analyzer (JNA) footprint along (a) 270°W and (b) 90°W.

of the sputtered neutral flux reflects that of the incident ion flux. Along the 270°W meridian (on the dayside/trailing hemisphere), the flux gradually decreases from latitudes ±60° to the equator, where the flux is minimal and four orders of magnitude lower than at +60°. We do note that while the results from Poppe's backwards-Liouville tracing model show a significantly higher flux at +60° than at −60° for the G8 flyby, a significant difference between the northern and southern hemispheres is not expected in reality.

On the 90°W meridian (on the nightside/leading hemisphere), the gradual decrease is interrupted at latitudes ±30° by narrow bands of intense sputtering, reflecting the narrow bands of intense ion precipitation in the incident flux (Figure 1). At these latitudes, the relative variation between adjacent zones is a factor of two to three. These large latitudinal variations show that ion precipitation patterns at the surface of Ganymede can be retrieved by remotely measuring ENAs.

4. Discussion

4.1. Variations Along Ganymede's Orbit

The ion precipitation distribution used here was simulated to reproduce the plasma environment at Ganymede during Galileo's G8 flyby when Ganymede was at the center of Jupiter's plasma sheet. Those results are in agreement with recent work by Plainaki et al. (2020), who additionally used MHD simulations to investigate the G2 and G28 flyby conditions, during which Ganymede was, respectively, above and below the center of the Jovian plasma sheet. Though simulations of sputtered ENA fluxes as a function of Ganymede's orbit are beyond the scope of this paper, Plainaki's recent work can be used together with our results to make a qualitative comment on expected sputtered ENA fluxes when Ganymede is above or below the center of Jupiter's plasma sheet.

Results from Plainaki et al. (2020) show overall decrease of ion precipitation fluxes in G2 and G28 conditions compared to G8. Assuming that, as observed in this work for the G8 flyby, ENA sputtering patterns are mostly correlated with ion precipitation patterns for the G2 and G28 cases, then we expect a significant decrease in sputtered ENA fluxes when Ganymede is outside the center of Jupiter's plasma sheet. The leading/trailing asymmetry of the precipitating ion flux observed at equatorial regions is a common feature of all three scenarios investigated by Plainaki et al. (2020), so we expect that intense ENA sputtering in polar regions and in the magnetotail (relative to equatorial regions) would remain a feature for G2 and G28 conditions as well as for G8 conditions investigated in this work. For conditions outside the plasma sheet, Plainaki et al. (2020) point out the existence of 'shielded areas' defined as 'regions with low or zero precipitation flux'. These shielded areas are large enough for G28 conditions that they create a North/South asymmetry, with intense flux to the South and shielding to the North on the leading hemisphere, and the reverse situation for the trailing hemisphere. We expect this North/South asymmetry to be a feature of sputtered ENA fluxes in G28 conditions as it is present for all three species considered by Plainaki et al. (2020).

4.2. Energy Distribution Models

In this study, we used a Thompson-Sigmund law to calculate the energy spectra of sputtered particles. In future work, the backscattering process should also be considered to more accurately simulate the energy spectra of ENAs to be observed at Ganymede. Backscattering is another process caused by precipitating ions, in which the impinging ion is neutralized (usually) and reflected by the surface. Measurements both in laboratories and in space suggest that backscattered particles would have energies in the range that JNA can measure, but distributed according to a Maxwell-Boltzmann-like law rather than the Thompson-Sigmund law applicable to sputtering (Futaana et al., 2012; Wieser et al., 2016). Backscattering yields are not well modeled, although studies by Wieser et al. (2016) and Futaana et al. (2012) suggest that a yield of about 0.1–0.2 can be applied for low (∼keV) energies. The majority of ENAs in the 10 eV - 1 keV range are produced by the sputtering process (by high energy particles), so the backscattered contribution to the total ENA spectra is expected to be small. Nevertheless, the different shape of their spectra may allow us to distinguish backscattered ENAs from sputtered ENAs.

Furthermore, nonlinear effects in the sputtering process expected at high energies (∼10 keVs) are not accounted for by the Thompson-Sigmund distribution. Indeed, Thompson-Sigmund is based on linear-cascade theory and accurately predicts the experimentally measured energy distribution of particles sputtered from various surfaces by projectiles with energies of up to 10s of keVs (e.g., Brizzolara et al., 1988; Goehlich, 2001; Haring et al., 1983; Thompson, 1968; Samartsev et al., 2005; Wieser et al., 2016). Measurements of energy distributions of particles sputtered by ∼MeV-energy projectiles from condensed gases (e.g., Johnson et al., 1983) only report low-energy sputtered products, typically less than 10 eV, perhaps due to limitations of measuring equipment. Consequently, there currently exists no adequate analytical model available that can accurately predict the experimentally measured energy distribution of particles sputtered from condensed gases by ∼MeV-energy projectiles.

For lack of a better model, the Thompson-Sigmund model has therefore been used here. Wieser et al. (2016) provides a good argument for the use of Thompson-Sigmund in our case as they successfully used it to fit the energy spectra, measured using a JNA prototype, of molecules sputtered from water ice under Ganymede surface-like conditions. Molecules with energies of up to 1.3 keV were observed under a 33 keV O^+ ion beam and followed a Thompson-Sigmund distribution. Thompson-Sigmund was also used in previous works to calculate the energy spectra of particles sputtered from airless body surfaces such as Mercury (Wurz & Lammer, 2003; Wurz et al., 2010), Europa (Plainaki et al., 2010, 2012; Vorburger & Wurz, 2018), and Ganymede (Plainaki et al., 2015), demonstrating the need for lab experiments that either validate its use or motivate the development of a better model. In any case, upon deployment in the Jovian environment, JNA will provide in-situ experimental energy spectra of atoms sputtered from icy moon surfaces. However, those data will be limited in resolution by the data and power budget of the JUICE spacecraft, further demonstrating the need for lab experiments such as those mentioned above, performed in controlled and repeatable conditions, to support the analysis of JNA data.

4.3. Angular Dependence

The angular distribution of sputtered particles has been predicted and measured to be $\cos^f(\theta)$, where θ is the angle relative to the surface normal and $f = 1$–2 depending on the target surface (Hofer, 2005). However, most of our results (global sputtering rates, sputtering maps, globally averaged energy spectra) are insensitive to the assumption we used in this work that the particles are sputtered isotropically. Only results relating to sputtered particles as observed by JNA would be affected by the isotropic assumption, but because JNA's field-of-view is small, and the overcosine distribution implies preferential sputtering in the direction of JNA (close to zenith), the effect is small (factor of 1.5–2).

5. Conclusion

We presented a new method to simulate the sputtering process at Ganymede, in order to estimate sputtered ENA fluxes to be observed by the Jovian Neutrals Analyzer, an ENA sensor to be deployed at Ganymede by ESA's upcoming JUICE mission. Our method combines three sputtering yield models to calculate the yield of H_2, O_2, and H_2O separately. Our global sputtering rates show that H_2 and O_2 account for half of the total global sputtering rate from Ganymede. Our total global sputtering rate is in agreement with previous works, but by separating each species, we were able to calculate their energy spectra, which is necessary in order to simulate JNA measurements.

Indeed, JNA's mass resolution only allows it to distinguish between H and heavier species, but information about the mass and origin of heavier species may be retrieved by looking at their energy spectra.

We also provided an estimate of expected JNA count rates and simulated the sputtered ENA flux at different locations along the track of a simplified orbit of the JUICE spacecraft. Our results show large latitudinal variations in sputtered ENA flux, demonstrating that JNA will be able to identify ion precipitation patterns by measuring ENAs. Future work will use realistic orbits of the JUICE spacecraft as well as JNA's calibrated instrument response, unavailable at the time of this study.

In conclusion, our results provide insight into the appearance of the data when JNA measures ENAs at Ganymede, as well as how the instrument should be operated optimally under limited power and data budget. The produced sputtering rate maps, energy spectra, and count rates in this study illustrate the capability of the ENA measuring technique to remotely map ion precipitation at Ganymede and provide clues for further potential ENA mapping in other icy bodies. Future work can easily use our model to produce more accurately simulated JNA spectra for different phases of the JUICE mission. Such simulations are crucial for optimizing operations planning and making the most of the limited integration time and data budget.

Data Availability Statement

Model results for this work are archived here: 10.528 1/zenodo.5607 581.

Acknowledgments
A. Pontoni acknowledges support from the Swedish National Space Agency, grant 189/16. S. Fatemi acknowledges support from the Swedish National Space Agency, grant 179/18. A. R. Poppe acknowledges support from NASA SSW grant #NNX16AR99G.

References

Allegrini, F., Dayeh, M. A., Desai, M. I., Funsten, H. O., Fuselier, S. A., Janzen, P. H., et al. (2013). Lunar energetic neutral atom (ENA) spectra measured by the interstellar boundary explorer (IBEX). *Planetary and Space Science*, *85*, 232–242. https://doi.org/10.1016/j.pss.2013.06.014

Barabash, S., Bhardwaj, A., Wieser, M., Sridharan, R., Kurian, T., Varier, S., et al. (2009). Investigation of the solar wind-Moon interaction onboard Chandrayaan-1 mission with the SARA experiment. *Current Science*, *96*, 526–532.

Baragiola, R., Vidal, R., Svendsen, W., Schou, J., Shi, M., Bahr, D., & Atteberrry, C. (2003). Sputtering of water ice. *Nuclear Instruments and Methods in Physics Research Section B: Beam Interactions with Materials and Atoms*, *209*, 294–303. https://doi.org/10.1016/S0168-583X(02)02052-9

Brizzolara, R. A., Cooper, C., & Olson, T. K. (1988). Energy distributions of neutral atoms sputtered by very low energy heavy ions. *Nuclear Instruments and Methods in Physics Research Section B: Beam Interactions with Materials and Atoms*, *35*(1), 36–42. https://doi.org/10.1016/0168-583X(88)90095-X

Carnielli, G., Galand, M., Leblanc, F., Modolo, R., Beth, A., & Jia, X. (2020). Simulations of ion sputtering at Ganymede. *Icarus*, *351*, 113918. https://doi.org/10.1016/j.icarus.2020.113918

Cassidy, T., Coll, P., Raulin, F., Carlson, R. W., Johnson, R. E., Loeffler, M. J., et al. (2010). Radiolysis and photolysis of icy satellite surfaces: Experiments and theory. *Space Science Reviews*, *153*(1–4), 299–315. https://doi.org/10.1007/s11214-009-9625-3

Cassidy, T., Paranicas, C., Shirley, J., Dalton, J., III, Teolis, B., Johnson, R., et al. (2013). Magnetospheric ion sputtering and water ice grain size at Europa. *Planetary and Space Science*, *77*, 64–73. https://doi.org/10.1016/j.pss.2012.07.008

Cooper, J. (2001). Energetic ion and electron irradiation of the icy Galilean satellites. *Icarus*, *149*(1), 133–159. https://doi.org/10.1006/icar.2000.6498

Famá, M., Shi, J., & Baragiola, R. (2008). Sputtering of ice by low-energy ions. *Surface Science*, *602*(1), 156–161. https://doi.org/10.1016/j.susc.2007.10.002

Fatemi, S., Poppe, A. R., Khurana, K. K., Holmström, M., & Delory, G. T. (2016). On the formation of Ganymede's surface brightness asymmetries: Kinetic simulations of Ganymede's magnetosphere. *Geophysical Research Letters*, *43*(10), 4745–4754. https://doi.org/10.1002/2016GL068363

Futaana, Y., Barabash, S., Grigoriev, A., Winningham, D., Frahm, R., Yamauchi, M., & Lundin, R. (2006). Global response of Martian plasma environment to an interplanetary structure: From Ena and plasma observations at Mars. *Space Science Reviews*, *126*(1), 315–332. https://doi.org/10.1007/s11214-006-9026-9

Futaana, Y., Barabash, S., Wieser, M., Holmström, M., Lue, C., Wurz, P., et al. (2012). Empirical energy spectra of neutralized solar wind protons from the lunar regolith: Empirical model OF backscattered Ena. *Journal of Geophysical Research*, *117*(E5). https://doi.org/10.1029/2011je004019

Futaana, Y., Barabash, S., Wieser, M., Lue, C., Wurz, P., Vorburger, A., et al. (2013). Remote energetic neutral atom imaging of electric potential over a lunar magnetic anomaly. *Geophysical Research Letters*, *40*(2), 262–266. https://doi.org/10.1002/grl.50135

Galli, A., Vorburger, A., Wurz, P., Cerubini, R., & Tulej, M. (2018). First experimental data of sulphur ions sputtering water ice. *Icarus*, *312*, 1–6. https://doi.org/10.1016/j.icarus.2018.04.029

Galli, A., Vorburger, A., Wurz, P., & Tulej, M. (2017). Sputtering of water ice films: A re-assessment with singly and doubly charged oxygen and argon ions, molecular oxygen, and electrons. *Icarus*, *291*, 36–45. https://doi.org/10.1016/j.icarus.2017.03.018

Goehlich, A. (2001). Investigation of time-of-flight and energy distributions of atoms and molecules sputtered from oxygen-covered metal surfaces by laser-aided techniques. *Applied Physics A Materials Science & Processing*, *72*(5), 523–529. https://doi.org/10.1007/s003390100810

Grundy, W. M., Buie, M. W., Stansberry, J. A., Spencer, J. R., & Schmitt, B. (1999). Near-infrared spectra of icy outer solar system surfaces: Remote determination of H_2O ice temperatures. *Icarus*, *142*(2), 536–549. https://doi.org/10.1006/icar.1999.6216

Gruntman, M. (1997). Energetic neutral atom imaging of space plasmas. *Review of Scientific Instruments*, *68*(10), 3617–3656. https://doi.org/10.1063/1.1148389

Haring, R., Haring, A., Klein, F., Kummel, A., & De Vries, A. (1983). Reactive sputtering of simple condensed gases by keV heavy ion bombardment. *Nuclear Instruments and Methods in Physics Research*, *211*(2–3), 529–533. https://doi.org/10.1016/0167-5087(83)90283-1

Hofer, W. O. (2005). *Angular, energy, and mass distribution of sputtered particles*. Springer Berlin Heidelberg. https://doi.org/10.1007/3540534288_16

Jia, X., Walker, R. J., Kivelson, M. G., Khurana, K. K., & Linker, J. A. (2008). Three-dimensional MHD simulations of Ganymede's magnetosphere: Ganymede MHD simulation. *Journal of Geophysical Research*, *113*(A6). https://doi.org/10.1029/2007ja012748

Johnson, R. E. (1990). *Energetic charged-particle interactions with atmospheres and surfaces*. Springer-Verlag. https://doi.org/10.1007/978-3-642-48375-2

Johnson, R. E., Boring, J. W., Reimann, C. T., Barton, L. A., Sieveka, E. M., Garrett, J. W., et al. (1983). Plasma ion-induced molecular ejection on the Galilean satellites: Energies of ejected molecules. *Geophysical Research Letters*, *10*(9), 892–895. https://doi.org/10.1029/GL010i009p00892

Johnson, R. E., Carlson, R. W., Cooper, J. F., Paranicas, C., Moore, M. H., & Wong, M. C. (2004). Radiation effects on the surfaces of the Galilean satellites. In *Jupiter: The planet, satellites and magnetosphere* (pp. 485–512).

Johnson, R. E., Quickenden, T. I., Cooper, P. D., McKinley, A. J., & Freeman, C. G. (2003). The production of oxidants in Europa's surface. *Astrobiology*, *3*(4), 823–850. https://doi.org/10.1089/153110703322736123

Kazama, Y., Barabash, S., Wieser, M., Asamura, K., & Wurz, P. (2007). Development of an LENA instrument for planetary missions by numerical simulations. *Planetary and Space Science*, *55*(11), 1518–1529. https://doi.org/10.1016/j.pss.2006.11.027

Khurana, K., Pappalardo, R., Murphy, N., & Denk, T. (2007). The origin of Ganymede's polar caps. *Icarus*, *191*(1), 193–202. https://doi.org/10.1016/j.icarus.2007.04.022

Leblanc, F., Oza, A. V., Leclercq, L., Schmidt, C., Cassidy, T., Modolo, R., et al. (2017). On the orbital variability of Ganymede's atmosphere. *Icarus*, *293*, 185–198. https://doi.org/10.1016/j.icarus.2017.04.025

Marconi, M. (2007). A kinetic model of Ganymede's atmosphere. *Icarus*, *190*(1), 155–174. https://doi.org/10.1016/j.icarus.2007.02.016

McComas, D. J., Allegrini, F., Bochsler, P., Frisch, P., Funsten, H. O., Gruntman, M., et al. (2009). Lunar backscatter and neutralization of the solar wind: First observations of neutral atoms from the Moon. *Geophysical Research Letters*, *36*(12). https://doi.org/10.1029/2009GL038794

Orton, G. S., Spencer, J. R., Travis, L. D., Martin, T. Z., & Tamppari, L. K. (1996). Galileo photopolarimeter-radiometer observations of Jupiter and the Galilean satellites. *Science*, *274*(5286), 389–391. https://doi.org/10.1126/science.274.5286.389

Paranicas, C., Cooper, J. F., Garrett, H. B., Johnson, R. E., & Sturner, S. J. (2009). Europa's radiation environment and its effects on the surface. *Europa, edited by Robert T. Pappalardo, William B. McKinnon, Krishan K. Khurana with the assistance of Ren_e Dotson with 85 collaborating authors* (p. 529). University of Arizona Press, The University of Arizona space science series.

Plainaki, C., Massetti, S., Jia, X., Mura, A., Milillo, A., Grassi, D., et al. (2020). Kinetic simulations of the Jovian energetic ion circulation around Ganymede. *The Astrophysical Journal*, *900*(1), 74. https://doi.org/10.3847/1538-4357/aba94c

Plainaki, C., Milillo, A., Massetti, S., Mura, A., Jia, X., Orsini, S., et al. (2015). The H_2O and O_2 exospheres of Ganymede: The result of a complex interaction between the Jovian magnetospheric ions and the icy moon. *Icarus*, *245*, 306–319. https://doi.org/10.1016/j.icarus.2014.09.018

Plainaki, C., Milillo, A., Mura, A., Orsini, S., & Cassidy, T. (2010). Neutral particle release from Europa's surface. *Icarus*, *210*(1), 385–395. https://doi.org/10.1016/j.icarus.2010.06.041

Plainaki, C., Milillo, A., Mura, A., Orsini, S., Massetti, S., & Cassidy, T. (2012). The role of sputtering and radiolysis in the generation of Europa exosphere. *Icarus*, *218*(2), 956–966. https://doi.org/10.1016/j.icarus.2012.01.023

Poppe, A. R., Fatemi, S., & Khurana, K. K. (2018). Thermal and energetic ion dynamics in Ganymede's magnetosphere. *Journal of Geophysical Research: Space Physics*, *123*(6), 4614–4637. https://doi.org/10.1029/2018JA025312

Roelof, E. C. (1987). Energetic neutral atom image of a storm-time ring current. *Geophysical Research Letters*, *14*(6), 652–655. https://doi.org/10.1029/GL014i006p00652

Samartsev, A. V., Duvenbeck, A., & Wucher, A. (2005). Sputtering of indium using Au m projectiles: Transition from linear cascade to spike regime. *Physical Review B*, *72*(11), 115417. https://doi.org/10.1103/PhysRevB.72.115417

Shematovich, V. I. (2016). Neutral atmosphere near the icy surface of Jupiter's moon Ganymede. *Solar System Research*, *50*(4), 262–280. https://doi.org/10.1134/S0038094616040067

Shimoyama, Asamura, K., Pontoni, A., Neuland, M. B., Karlsson, S., Wieser, M., et al. (2018). *Jovian neutrals analyzer for the particle environment package onboard JUICE*.

Siscoe, G. L., Eviatar, A., Thorne, R. M., Richardson, J. D., Bagenal, F., & Sullivan, J. D. (1981). Ring current impoundment of the Io plasma torus. *Journal of Geophysical Research*, *86*(A10), 8480–8484. https://doi.org/10.1029/JA086iA10p08480

Siscoe, G. L., & Summers, D. (1981). Centrifugally driven diffusion of iogenic plasma. *Journal of Geophysical Research*, *86*(A10), 8471–8479. https://doi.org/10.1029/JA086iA10p08471

Teolis, B. D., Plainaki, C., Cassidy, T. A., & Raut, U. (2017). Water ice radiolytic O_2, H_2, and H_2O_2 yields for any projectile species, energy, or temperature: A model for icy astrophysical bodies. *Journal of Geophysical Research: Planets*, *122*(10), 1996–2012. https://doi.org/10.1002/2017JE005285

Thompson, M. W. (1968). II. The energy spectrum of ejected atoms during the high energy sputtering of gold. *Philosophical Magazine*, *18*(152), 377–414. https://doi.org/10.1080/14786436808227358

Turc, L., Leclercq, L., Leblanc, F., Modolo, R., & Chaufray, J.-Y. (2014). Modelling Ganymede's neutral environment: A 3D test-particle simulation. *Icarus*, *229*, 157–169. https://doi.org/10.1016/j.icarus.2013.11.005

Vorburger, A., & Wurz, P. (2018). Europa's ice-related atmosphere: The sputter contribution. *Icarus*, *311*, 135–145. https://doi.org/10.1016/j.icarus.2018.03.022

Vorburger, A., Wurz, P., Barabash, S., Wieser, M., Futaana, Y., Holmström, M., & Asamura, K. (2014). First direct observation of sputtered lunar oxygen. *Journal of Geophysical Research: Space Physics*, *119*(2), 709–722. https://doi.org/10.1002/2013JA019207

Wieser, M., Barabash, S., Futaana, Y., Holmström, M., Bhardwaj, A., Sridharan, R., & Asamura, K. (2009). Extremely high reflection of solar wind protons as neutral hydrogen atoms from regolith in space. *Planetary and Space Science*, *57*(14–15), 2132–2134. https://doi.org/10.1016/j.pss.2009.09.012

Wieser, M., Futaana, Y., Barabash, S., & Wurz, P. (2016). Emission of energetic neutral atoms from water ice under Ganymede surface-like conditions. *Icarus*, *269*, 91–97. https://doi.org/10.1016/j.icarus.2015.12.043

Wurz, P., & Lammer, H. (2003). Monte-Carlo simulation of Mercury's exosphere. *Icarus*, *164*(1), 1–13. https://doi.org/10.1016/S0019-1035(03)00123-4

Wurz, P., Whitby, J., Rohner, U., Martín-Fernández, J., Lammer, H., & Kolb, C. (2010). Self-consistent modelling of Mercury's exosphere by sputtering, micro-meteorite impact and photon-stimulated desorption. *Planetary and Space Science*, *58*(12), 1599–1616. https://doi.org/10.1016/j.pss.2010.08.003